Received: 6 November 2018 | Revised: 16 January 2019 | Accepted: 18 January 2019

DOI: 10.1002/gj.3473

RESEARCH ARTICLE

WILEY

$^{40}Ar/^{39}Ar$ geochronology, fluid inclusions, and ore-grade distribution of the Jiawula Ag–Pb–Zn deposit, NE China: Implications for deposit genesis and exploration

Si-Da Niu[1,2,3] | Sheng-Rong Li[3,4] | Jan Marten Huizenga[5,6] | M. Santosh[4,7] | De-Hui Zhang[4] | Zeng-Da Li[8,3]

[1] Institute of Mineral Resources Research, China Metallurgical Geology Bureau, Beijing, China

[2] Department of Geology, Northwest University, Xi'an, China

[3] State Key Laboratory of Geological Processes and Mineral Resources, China University of Geosciences, Beijing, China

[4] School of Earth Science and Resources, China University of Geosciences, Beijing, China

[5] Economic Geology Research Institute (EGRU), College of Science and Engineering, James Cook University, Townsville, Queensland, Australia

[6] Department of Geology, University of Johannesburg, Auckland Park, Johannesburg, South Africa

[7] Department of Earth Sciences, University of Adelaide, Adelaide, South Australia, Australia

[8] Department of Exploration Technology, Minmetals Exploration and Development Co., Ltd, Beijing, China

Correspondence
Sheng-Rong Li, School of Earth Science and Resources, China University of Geosciences Beijing, 29 Xueyuan Road, Beijing 100083, China.
Email: lisr@cugb.edu.cn

Funding information
China Geological Survey, Grant/Award Number: 12120114051101; National Key Research and Development Program of China, Grant/Award Number: 2016YFC0600210

Handling Editor: L. Tang

The Jiawula Ag–Pb–Zn deposit is located in the northern part of the Great Xing'an Range metallogenic belt within the eastern segment of the Central Asian Orogenic Belt. Here, we report results from muscovite $^{40}Ar/^{39}Ar$ geochronology and fluid inclusion study and formulate a vertical projection map of the ore grade in this deposit. The muscovite from the Jiawula deposit yields a plateau age of 133.27 ± 0.66 Ma and a $^{40}Ar/^{39}Ar$ isochron age of 131.88 ± 0.83 Ma. The muscovite $^{40}Ar/^{39}Ar$ data indicate a discrete second hydrothermal event postdating the mineralization, which we correlate with post-collisional extension after the subduction direction of the Palaeo-Pacific Plate changed. Low-salinity aqueous fluid inclusions in quartz from the Jiawula deposit represent meteoric water or groundwater. Based on the fluid inclusion study, the fluids were trapped during cooling and decompression, which may have resulted in metal precipitation. We envisage that the copper precipitated from a high-temperature fluid in the southern domain whereas lead, zinc, and silver precipitated at a lower temperature in the north. The spatial distribution of the ore-forming elements, therefore, reflects the ore fluid migration-cooling path from the south to north.

KEYWORDS

$^{40}Ar/^{39}Ar$ geochronology, deposit genesis, exploration, fluid evolution and migration, Jiawula Ag–Pb–Zn deposit, ore deposit modelling

1 | INTRODUCTION

The Great Xing'an Range, located in the eastern segment of the Central Asian Orogenic Belt, is an important polymetallic belt in north-eastern China. It hosts different types of Mesozoic base and precious metal deposits, including porphyry, skarn, hydrothermal vein, and epithermal type (Chen, Zhang, Li, Yang, & Deng, 2012; Liu et al., 2014; Zhai et al., 2012). Previous geochronological studies indicate

that the mineralization in this region formed during the Late Mesozoic and peaked during the Early Cretaceous (Bai, Sun, Gu, Zhao, & Sun, 2014; Mao et al., 2013; Mao, Wang, Zhang, Yu, & Niu, 2003; Ouyang et al., 2013; Zhou et al., 2015, 2009; Zhou, Mao, & Lyckberg, 2012). The Jiawula Ag–Pb–Zn deposit is located in the northern part of the great Xing'an Range metallogenic belt, which forms the extension of the well-known Russian–Mongolian polymetallic metallogenic belt. Closely related to the volcanic–subvolcanic activities, the Jiawula deposit is considered as an epithermal deposit (Niu et al., 2017; Zhai, Liu, Wang, Yao, Liu, et al., 2013; Zhai, Liu, Wang, Yao, Wu, et al., 2013).

Previous studies on the Jiawula deposit mainly focused on the deposit geology (Zeng, 2010), exploration geochemistry (Zhao, Sun, Jing, & Wang, 2005), metallogenic fluid characteristics (Li et al., 2015; Wu, Mi, Gao, Li, & Qiao, 2010; Zhai, Liu, Wang, Yao, Liu, et al., 2013; Zhai, Liu, Wang, Yao, Wu, et al., 2013), mineralogy and isotopic studies (Niu et al., 2016), zircon U–Pb geochronology, and geochemistry of the intrusions (Niu et al., 2017).

In spite of several previous studies, issues concerning the genesis and tectonic implications of the Jiawula deposit remain unresolved including the number of hydrothermal or epithermal events, the nature of the mineralizing fluid, and the spatial distribution of the metallogenic elements. The source and mechanism of precipitation of the ore-forming elements are also controversial (Li et al., 2015; Zhai, Liu, Wang, Yao, Wu, et al., 2013). In this paper, we present the results from (a) $^{40}Ar/^{39}Ar$ geochronology on muscovite, (b) detailed fluid inclusion study, and (c) geochemical prospecting in order to address some of the outstanding issues.

2 | REGIONAL GEOLOGY

The Great Xing'an Range is located in the eastern segment of the Central Asian Orogenic Belt (CAOB) which marks the boundary between the Siberian, Tarim, and North China cratons (Figure 1a). The Jiawula deposit occurs within the Ulaan-Jiawula metallogenic province, which comprises densely distributed mineralization including 44 superlarge and large deposits (Nie, Li, Liu, & Ding, 2015; Zhao, Xu, & Zhang, 2017). The Ulaan-Jiawula metallogenic province forms part of the Erguna orogenic belt, which is located in the northern extremity of the Great Xing'an Range to the north-west of the Derbugan Fault (Figure 1b).

Two major tectono-stratigraphic units were recognized in the Great Xing'an Range: a pre-Jurassic metamorphic massif and a Mesozoic volcano-sedimentary sequence (Kröner et al., 2014; Nie et al., 2015; Zhou & Wilde, 2013). The local stratigraphy is dominated by Jurassic successions and, to a lesser extent, Cretaceous rocks (Figure 1c). Metallic mineralization including Cu, Ag, Pb, Zn, and Mo occurs within intermediate-mafic volcanic rocks of the Tamulangou Formation and sedimentary units including sandstone and conglomerate of the Nanping Formation (Zhai, Liu, Wang, Yao, Wu, et al., 2013).

The Great Xing'an Range records strong superimposition and transition between the east–west trending Palaeozoic Palaeo-Asian domain and the south-south-west and north-north-east trending Mesozoic–Cenozoic western Pacific tectonic/metallogenic domain. The main tectonic events of this region belong to two distinct stages: (a) north–south trending compression between the Siberian Craton and the North China Craton prior to Early Jurassic, and (b) oblique north-west subduction of the Pacific Plate towards the east of the Eurasian continent beginning in the Middle–Late Jurassic (Liu et al., 2014; Mao et al., 2005; Mao et al., 2013; Wilde & Zhou, 2015). The north-east and north-west trending conjugate faults formed during pre-Mesozoic and played an important role both in the development of the regional structural architecture and in controlling the magmatic and metallogenic activities (Hu, Yan, Ye, & Xiang, 1998).

Widespread magmatism in the form of multiphase plutonic and volcanic activities took place across the Great Xing'an Range. Mafic and ultramafic rocks mainly formed in the Late Palaeozoic and were mostly developed along the boundaries between the blocks. Massive intermediate and felsic intrusions were emplaced in the Late Palaeozoic and Mesozoic (Liu, Zhang, & Zhang, 2004). The Erguna Block shows evidence for four stages of granitic magmatism: Neoproterozoic (851–737 Ma), Early Palaeozoic (*ca*. 490 Ma), Early–Middle Jurassic (200–160 Ma), and Early Cretaceous (*ca*. 130 Ma). The Neoproterozoic and Early Palaeozoic granitoids occur scattered within the widespread Triassic–Jurassic plutons that range in age from 241 to 182 Ma (Ouyang et al., 2013; Tang et al., 2014; Tang, Xu, Wang, Zhao, & Wang, 2016; Wu et al., 2011).

Mesozoic magmatism shows a close temporal-spatial relationship with mineralization. Igneous bodies were emplaced in a shallow crustal setting as mid-hypabyssal, hypabyssal, and ultra-hypabyssal intrusions with felsic and intermediate compositions (Li et al., 2014; Niu et al., 2017). The main rock types include dacite porphyry, granite porphyry, quartz porphyry, and quartz monzonite porphyry (Nie et al., 2015; Niu et al., 2017; Zhai, Liu, Wang, Yao, Wu, et al., 2013).

3 | DEPOSIT GEOLOGY

The Jiawula deposit occurs 45 km north-west of Xin Barag Right Banner and 150 km south-west from Manzhouli City. The stratigraphy is dominated by Jurassic successions, composed of Middle Jurassic sandstone and conglomerate of the Nanping Formation, andesite and basaltic andesite of the Tamulangou Formation, and Upper Jurassic andesite and rhyolite of the Shangkuli Formation (Figure 2). Almost all of the ores are hosted by Jurassic rocks of the Tamulangou and Nanping formations.

The widely distributed magmatic rocks are mainly Late Permian to Early Triassic and Late Jurassic. The *ca*. 254–247 Ma intrusions are composed of granodiorite (254 ± 2 Ma), dacite porphyry (252.9 ± 4.8 Ma), and diorite porphyry (278 ± 4.1 Ma), whereas the 150–145 Ma granitoids comprise quartz porphyry (150.1 ± 1.8 Ma), syenite porphyry (148.8 ± 2.2 Ma), and monzonite porphyry (145.3 ± 1.9 Ma; Niu et al., 2017). The Early Cretaceous metallogenic event is slightly younger than the Late Jurassic magmatic event as exemplified by the Rb–Sr age of quartz in the Pb–Zn ores (140.0 ± 11.0 Ma; Wang et al., 2010), and the Rb–Sr age of sphalerite and pyrite (142.7 ± 1.3 Ma; Li et al., 2014).

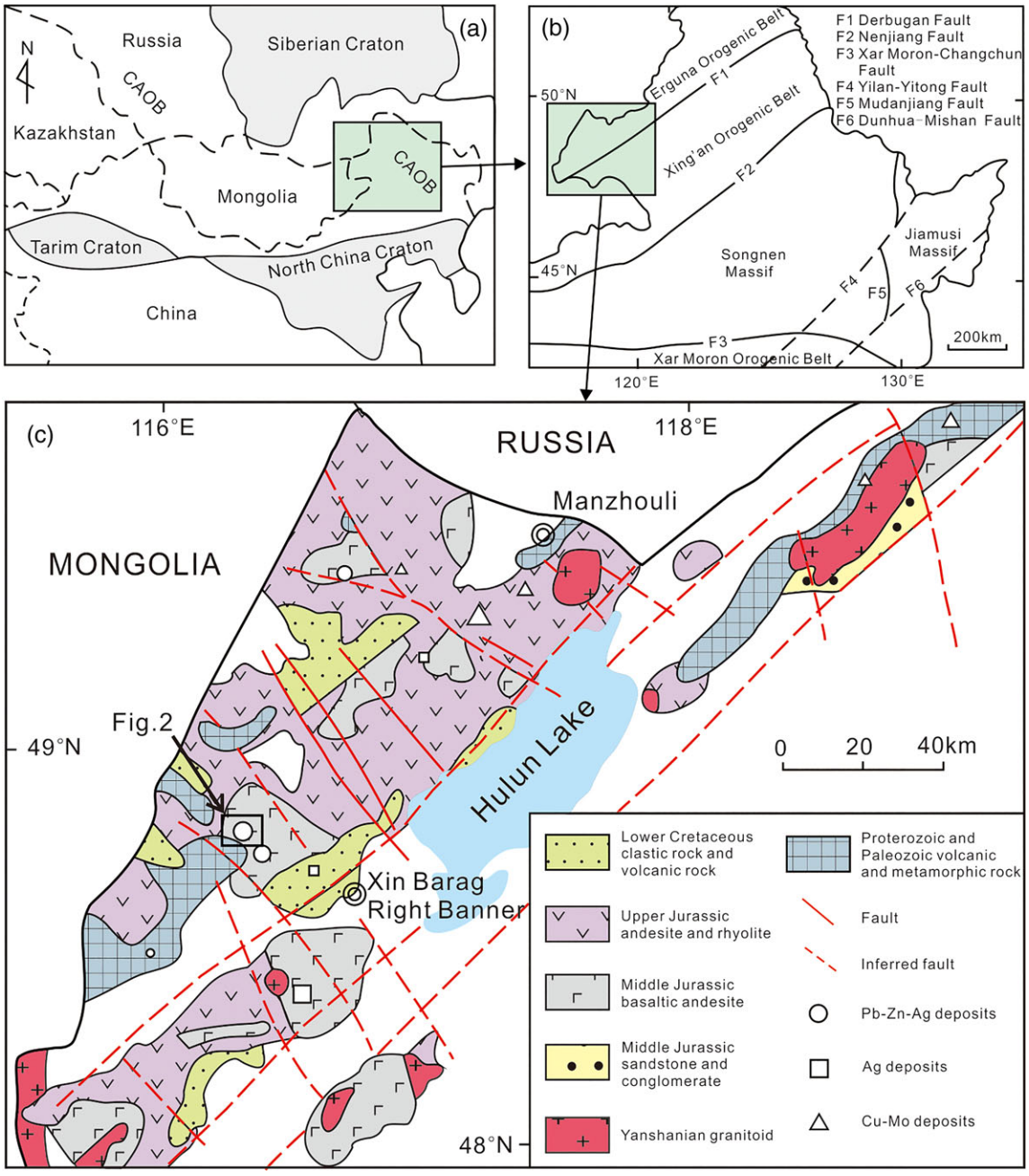

FIGURE 1 Regional geological setting and geology of the Manzhouli area in the northern part of the Great Xing'an Range. (a) Location of the Central Asian Orogenic Belt with respect to surrounding cratons. (b) After Figure 1 from Ge, Wu, Zhou, & Abdel Rahman, 2005. (c) After Figure 1 from Wu et al., 2006 [Colour figure can be viewed at wileyonlinelibrary.com]

The north-west and north-north-west trending faults have a genetic relationship with the volcanic edifice and control the distribution of ore bodies (Li et al., 2014). More than 40 ore bodies have been identified in the Jiawula Ag–Pb–Zn deposit, most of which occur as veins. The ore bodies occur in close proximity to the feldspar porphyry and quartz porphyry intrusions and are found within the fracture zones and along the intrusion boundaries. The orebodies show a variable dip angle (42–70°) to the south-west with a general strike direction of 330–350°. The Jiawula deposit comprises five main ore bodies, numbered 1, 2, 3, 4, and 12, among which the No. 2 ore body is the largest extending for over 2 km laterally, 300–500 m in depth and with a thickness of 0.4–15 m (average 3.9 m). The mean grade of the deposit is 2.65% Pb, 4.24% Zn, 0.30% Cu, and 124.31 g/t Ag (Zhai, Liu, Wang, Yao, Wu, et al., 2013).

The major ore minerals of the Jiawula deposit include pyrite, sphalerite, galena, chalcopyrite, arsenopyrite, magnetite, and argentite. Quartz, chlorite, calcite, rhodochrosite, muscovite, and fluorite are the main gangue minerals. Sericite, amphibole, and barite are also present in minor amounts. The ore textures are mostly idiomorphic or hypidiomorphic (Figure 3a,e), and xenomorphic (Figure 3b–d), with massive (Figure 3b), brecciated (Figure 3c,d), vein, disseminated, and banded structures (Niu et al., 2017).

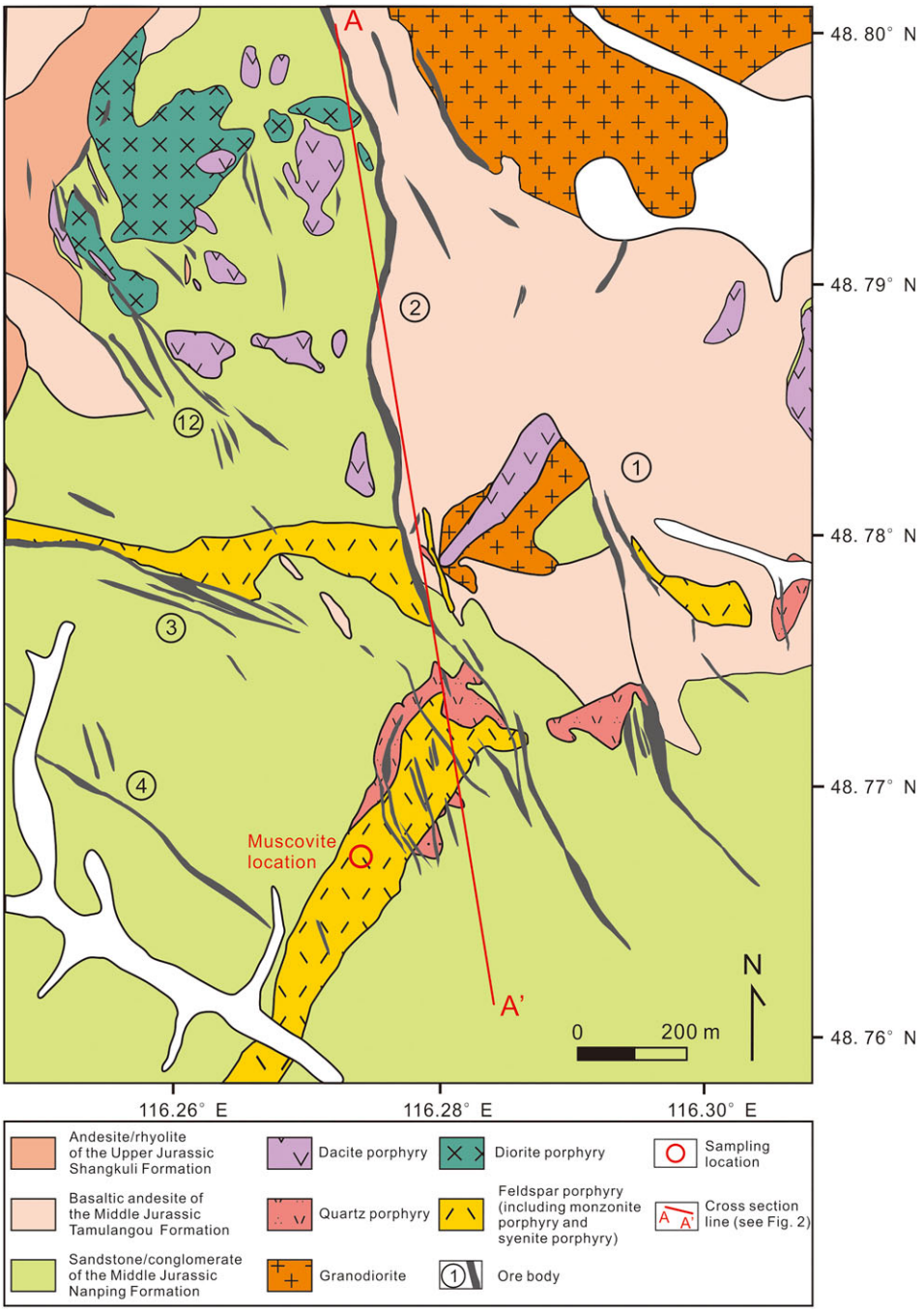

FIGURE 2 Geological map of the Jiawula deposit (modified from Zhai, Liu, Wang, Yao, Liu, et al., 2013) [Colour figure can be viewed at wileyonlinelibrary.com]

4 | SAMPLING AND METHODOLOGY

4.1 | Muscovite sampling and analytical methods

The muscovite sample was collected from the Jiawula deposit (location shown on Figure 2) hosted in andesite. The yellow-green muscovite forms aggregates of coarse-grained (grain size of 5–10 mm) euhedral crystals coexisting with fluorite (Figure 3a,f,g). Electron microprobe analysis of the muscovite was done on a JEOL JXA-8230 electron microprobe at the Chinese Academy of Geological Sciences (CAGS). Measurements were performed by Wavelength Dispersive Spectroscopy (WDS), using an accelerating voltage of 15 kV, a specimen current of 20 nA, and a beam diameter of 5 μm.

The muscovite sample was crushed to −20 mesh, from which the mica flakes were separated using conventional heavy liquid and magnetic techniques, followed by ultrasonic cleaning. About 0.2 g of the muscovite flakes were handpicked under a binocular microscope to avoid contamination. Muscovite grains for $^{40}Ar/^{39}Ar$ dating were irradiated with fast neutrons for 62 hr at the Geoanalytical Center of Nuclear Industry (GCNI) and subsequently cooled for about 100 days. $^{40}Ar/^{39}Ar$

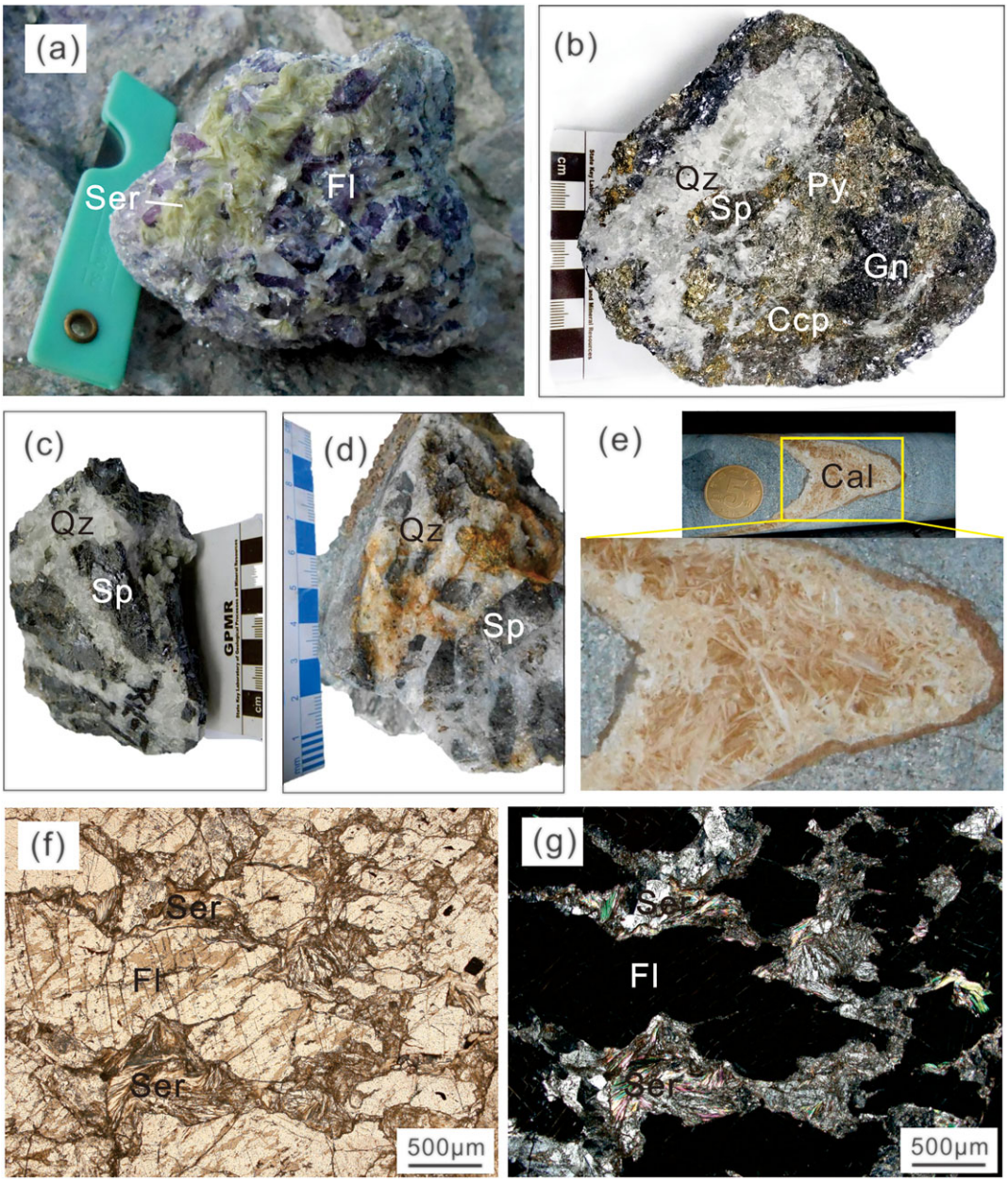

FIGURE 3 Representative hand specimens of the Jiawula Ag–Pb–Zn deposit. (a) Paragenesis of sericite and fluorite. (b) Disseminated ore, showing the intergrowth of quartz, pyrite, sphalerite, galena, and chalcopyrite. (c,d) Brecciated sphalerite ore filled with quartz veins. (e) Calcite with lattice texture. (f) Sericite coexisting with fluorite (plane-polarized light). (g) Sericite coexisting with fluorite (cross-polarized light). Ser: sericite; Fl: fluorite; Qz: quartz; Sp: sphalerite; Gn: galena; Ccp: chalcopyrite; Py: pyrite; Cal: calcite [Colour figure can be viewed at wileyonlinelibrary.com]

stepwise heating analyses were performed at the GCNI using an Argus VI-MC mass spectrometer. Samples were analysed in 11 temperature steps from 300°C to total fusion at 1300°C. The biotite standard JBH (132.5 Ma) was used to monitor the neutron flux. $^{40}Ar/^{39}Ar$ plateau ages were calculated using ISOPLOT 3.00 (Ludwig, 2004).

4.2 | Fluid inclusion sample selection and analytical methods

Two quartz samples (Samples 2-25 and 7-7) from ores of the Jiawula deposit were selected for fluid inclusion study. The quartz is intergrown with sphalerite, galena, chalcopyrite, and pyrite and thus associated with the mineralization event (Figure 3b,c).

Fluid inclusion petrography and microthermometry were carried out on doubly polished samples (*ca*. 200 μm thick) using a Linkam heating–freezing stage. The stage is attached to an Olympus BX51 microscope with a maximum objective magnification of 50. The stage is controlled by Linksys32 software, which allows heating and cooling rates between 0.1°C/min and 90°C/min. An infrared filter is used to minimize the heating effect of light source on the sample. Pure CO_2 and H_2O fluid inclusions in quartz were used for calibration at the triple points of CO_2 (−56.6°C) and H_2O (0.0°C). Critical homogenization temperatures of synthetic H_2O inclusions in quartz were used for

calibration at 374°C. In this study, only aqueous liquid-vapour fluid inclusions were found. The measured melting (Tm) and homogenization temperatures (Th) have an accuracy of ±0.2°C and ± 5°C, respectively. Phase transitions that were measured during heating include initial melting, final melting of ice, and homogenization of the vapour bubble into the liquid phase. Salinity, density, and isochores for H_2O-NaCl fluid inclusions were calculated using Hokie_Flincs_H2O-NaCl (Steele-Macinnis, Lecumberri-Sanchez, & Bodnar, 2012).

4.3 | Methodology of vertical ore grade projection map

The No. 2 ore body is the largest one in the Jiawula deposit (location shown in Figure 2) as its reserve accounts for more than 80% of the total. A total of 85 samples were collected from this ore body, which were subsequently chemically analysed for lead, zinc, silver, and copper (Table S1). The sampling location is shown in Figure 4a, and the contour maps are presented in Figure 4b–e. Complexometric titration method is used for chemical analysis (Ding, 2004). A vertical longitudinal projection based on the contents of main ore-forming elements (lead, zinc, silver, and copper) was carried out in order to delineate geochemical anomalies (Zheng, 1991). The SURFER software was used to delineate the geochemical anomaly concentration patterns based on the conventional gradient concept.

5 | MUSCOVITE GEOCHRONOLOGY

5.1 | Mineral chemistry of the muscovite

The chemical compositions of the mica in the Jiawula deposit are shown in Table 1. The calculated molecular formula of the mica is $(K_{0.75}, Na_{0.01})_{0.76}$, $(Al_{2.08}, Mg_{0.05}, Fe_{0.10}, Ti_{0.01})_{2.24}$ $[(Si_{3.37}, Al_{0.63})_{4.00}O_{10}](OH_{1.53}, Cl_{0.01}, F_{0.46})_{2.00}$. Based on the classification of Foster (1960), the mica in the Jiawula deposit can be classified as muscovite (Figure 5).

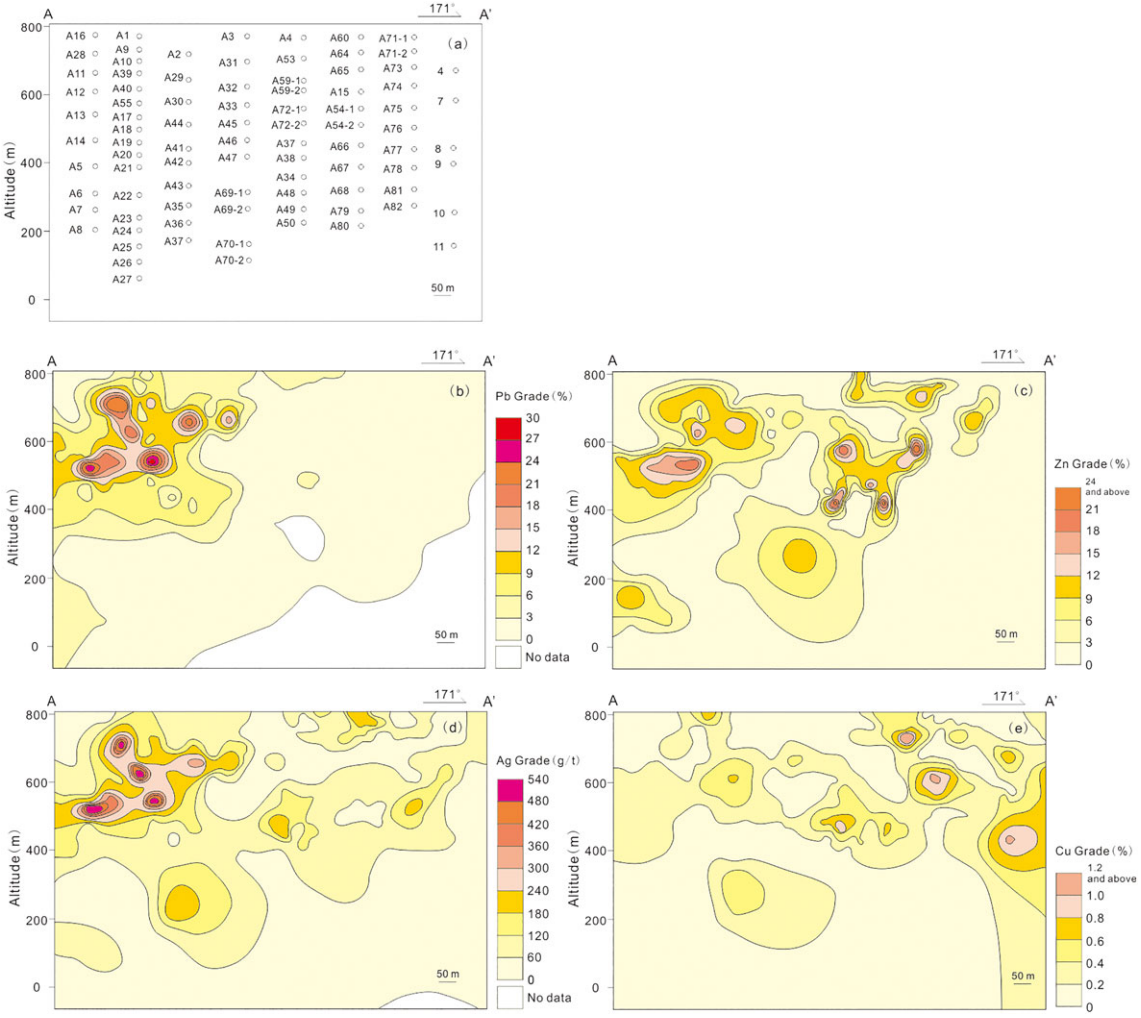

FIGURE 4 Sampling location (a) and vertical longitudinal projection of the anomalous metal concentration of lead (b), zinc (c), silver (d), and copper (e) of the No. 2 ore body (section A-A′ shown in Figure 2) [Colour figure can be viewed at wileyonlinelibrary.com]

TABLE 1 Representative EPMA results of the muscovite from the Jiawula deposit

Sample no.	SiO_2	TiO_2	Al_2O_3	FeO	MnO	MgO	CaO	Na_2O	K_2O	F	Cl	Total
JWL-8-1	50.81	0.11	33.86	2.34	0.08	0.91	bdl	0.17	8.89	0.56	bdl	97.74
JWL-8-1	51.89	0.01	35.41	1.80	0.06	0.52	bdl	0.11	9.13	0.40	bdl	99.32
JWL-8-1	51.87	bdl	34.66	1.53	0.08	0.78	0.01	0.15	9.07	0.25	0.01	98.41
JWL-8-1	51.46	0.08	33.16	1.37	0.07	1.18	0.02	0.09	8.53	0.73	bdl	96.69
JWL-8-1	49.32	bdl	33.94	1.81	0.03	0.37	bdl	0.14	9.38	0.51	bdl	95.49

Note. bdl: below detection limit.

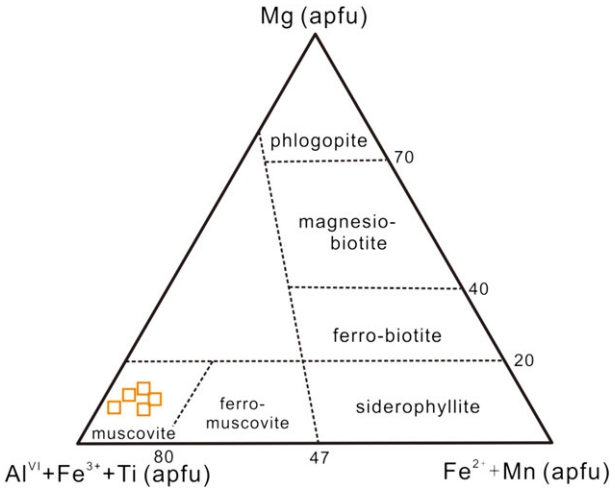

FIGURE 5 Classification of mica in the Jiawula deposit intrusives (after Foster, 1960). apfu: atoms per formula unit [Colour figure can be viewed at wileyonlinelibrary.com]

5.2 | $^{40}Ar/^{39}Ar$ dating results

The analytical results and the corresponding plateau age and isochron age are shown in Figure 6 and summarized in Table 2. The muscovite from the Jiawula deposit yields a plateau age of 133.27 ± 0.66 Ma (Figure 6a; MSWD = 0.72). The muscovite separates yield a $^{40}Ar/^{39}Ar$ isochron age of 131.88 ± 0.83 Ma defined by all the 15 gas emissions (MSWD = 0.21) with initial $^{40}Ar/^{36}Ar$ values of 421.7 ± 46.0 (Figure 6b).

6 | FLUID INCLUSION STUDY

6.1 | Petrography and fluid inclusion type

The main objective of the fluid inclusion study is to identify the fluid that was present during ore formation, and therefore, we mainly focus on fluid inclusions that were formed during crystal growth. For that reason, domains that are characterized by the occurrence of isolated and clustered fluid inclusions were selected for this study (Figure 7a,b).

Two fluid inclusion types were identified in the selected areas. Type 1 appears as 10–20 μm sized transparent (colourless) regular (sometimes near negative-crystal shape) shaped fluid inclusions. They comprise a liquid and a vapour phase at room temperature (Figure 7c), in which the water volume fraction is greater than that of the vapour phase. These fluid inclusions homogenize into liquid phase during heating and are the most abundant ones, accounting for more than 95% of all fluid inclusions.

Type 2 fluid inclusions are vapour-rich (Figure 7d), comprising liquid water having lesser volume than that of the vapour phase at room temperature. The phase change of the vapour-rich fluid inclusions in the Jiawula deposit could not be observed during freezing or heating. Besides, the vapour-rich fluid inclusions appear only sporadically, so we identified them as the product of explosion after the original forming process of the mineral. Therefore, this fluid inclusion type was considered to be irrelevant in this study.

6.2 | Microthermometry results

Both samples show consistent results for melting and homogenization temperatures in this study. The homogenization temperatures of Sample 2-25 range between 155°C and 286°C, whereas those of Sample 7-7 range between 169°C and 286°C (Table 3; Figure 8a). Initial melting was observed to occur at a temperature of *ca*. −20°C to −25°C, corresponding to the eutectic temperature for the H_2O-NaCl system (−21.1°C). The final ice melting temperature of fluid inclusions in both samples ranges between −1.4°C and − 0.2°C (Table 3; Figure 8b), corresponding to the salinity ranging between 2.4 and 0.4 wt% NaCl. The plot diagram of the salinity and homogenization temperature is shown in Figure 9, and the isochores are shown in Figure 10.

7 | VERTICAL ORE GRADE PROJECTION MAP

The trend of No. 2 ore body is 320–350°, dipping 55–65° to the south-west. The vertical longitudinal projection is based on the cross-section A-A′ (Figure 2). The lead distributions in the southern and the northern part of the ore body are significantly different. The lead grade contour map (Figure 4b) reflects the concentration of lead in the shallow northern part of the No. 2 ore body at an elevation of 400–800 m.

The zinc and lead distributions in the No. 2 ore body have both overlapping features and obvious differences. There are high value centers both in the north and middle section on the projection for zinc (Figure 4c), whereas lead is concentrated in the north.

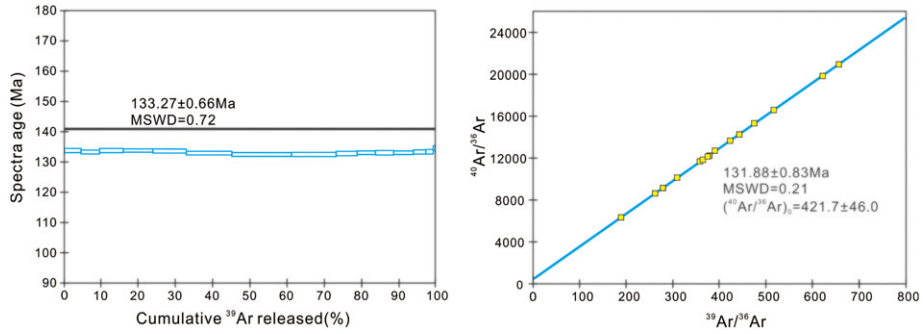

FIGURE 6 ^{40}Ar/^{39}Ar plateau (a) and corresponding isochron (b) ages for muscovite analysed by laser ablation [Colour figure can be viewed at wileyonlinelibrary.com]

TABLE 2 ^{40}Ar/^{39}Ar laser ablation dating results for the muscovite from the Jiawula deposit

Heating step (°C)	$(^{40}Ar/^{39}Ar)_m$	$(^{36}Ar/^{39}Ar)_m$	$(^{37}Ar/^{39}Ar)_m$	^{40}Ar (%)	$F(^{40}Ar^*/^{39}Ar)$	^{39}Ar(×10^{-14} mol)	^{39}Ar(Cum.) (%)	Age (Ma)	±1σ (Ma)
650	32.5255	0.0028	0.0197	97.46	31.7014	3.75	4.70	133.79	0.66
700	32.3792	0.0028	0.0536	97.50	31.5703	4.02	5.03	133.25	0.65
750	32.4511	0.0026	0.0402	97.67	31.6949	4.99	6.24	133.76	0.66
800	32.6673	0.0032	0.0021	97.07	31.7113	6.39	8.01	133.83	0.66
850	32.8031	0.0038	0.0017	96.56	31.6756	7.18	8.99	133.68	0.66
900	32.2610	0.0026	0.0018	97.58	31.4805	9.74	12.19	132.89	0.66
950	31.8579	0.0016	0.0025	98.51	31.3823	12.77	15.99	132.49	0.65
1000	31.8403	0.0015	0.0046	98.58	31.3898	9.62	12.04	132.52	0.64
1050	32.0259	0.0019	0.0093	98.21	31.4544	4.44	5.55	132.78	0.65
1100	32.1697	0.0023	0.0050	97.92	31.5019	3.95	4.94	132.97	0.65
1150	32.3101	0.0027	0.0076	97.56	31.5230	3.92	4.91	133.06	0.65
1200	32.2051	0.0024	0.0083	97.83	31.5067	4.26	5.33	132.99	0.66
1250	32.2124	0.0021	0.0138	98.07	31.5904	2.72	3.40	133.33	0.66
1300	32.6494	0.0036	0.0612	96.76	31.5925	1.52	1.90	133.34	0.66
1400	33.4474	0.0053	0.2398	95.33	31.8921	0.61	0.77	134.56	0.68

The silver grade contour map (Figure 4d) illustrates that silver is also relatively concentrated in the northern section of the No. 2 ore body. The northern concentration area of silver, lead, and zinc is almost identical. By contrast, copper is more concentrated in the south and shows an increasing concentration towards the south (Figure 4e).

8 | DISCUSSION

8.1 | Significance of the muscovite ^{40}Ar/^{39}Ar dating

The ^{40}Ar/^{39}Ar dating method can be applied to date metallogenic events, provided that (a) mica and metal-bearing minerals are from the same paragenetic mineral assemblage; (b) no significant thermotectonic event occurred after formation of mica as the ^{40}Ar/^{39}Ar system can be disturbed in mica at temperatures greater than 350°C; and (c) the effect of excess argon is negligible (McDougall & Harrison, 1999; Zheng, Zhang, Chen, Hollings, & Chen, 2013). The data from the sample we studied in the Jiawula deposit show only a narrow closure temperature range, and is thus not very susceptible to the incorporation of excess argon. However, mica rarely coexists with the ore minerals, showing paragenesis with fluorite (Figure 3a). Therefore, the *ca.* 133–131 Ma age of the muscovite does not represent the mineralization age of the Jiawula deposit.

Previous studies reported the mineralization age of the Jiawula deposit from Rb–Sr isochron age of sphalerite in the ores as 143.0 ± 2.0 Ma, and that from pyrite as 142.7 ± 1.3 Ma, marking an Early Cretaceous mineralization event (Li et al., 2014). The 145.3 ± 1.9 Ma age of monzonite porphyry confirms that mineralization followed the major magmatic phase (Niu et al., 2017). No reasonable field and petrological evidences were found for multistage mineralization events. Further, the cooling rates were estimated to be 100°C/m.y. (Selby et al., 2002), and the life span of a typical intrusion-related hydrothermal system is considered to be short and no more than 1 million years (Cathles, Erendi, & Barrie, 1997; Marsh, Einaudi, & McWilliams, 1997; Ronacher, Richards, Villeneuve, & Johnston, 2002). Considering the fact that mineralization occurred at *ca.* 143 Ma, the plateau age of 133.27 ± 0.66 Ma and the isochron

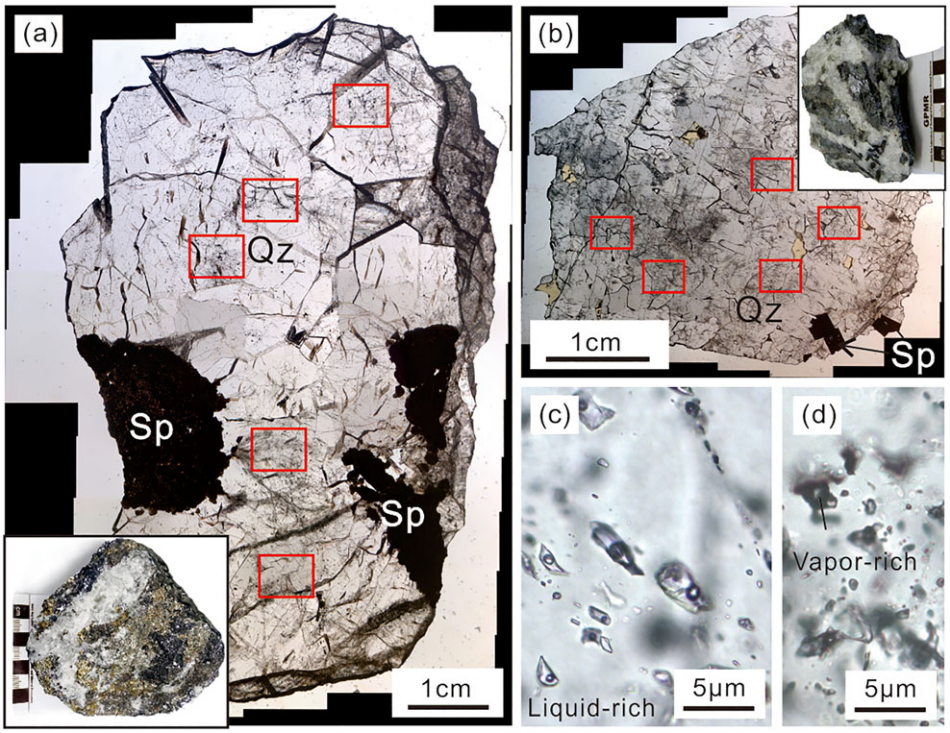

FIGURE 7 Fluid inclusion petrology and fluid inclusion types in quartz from the Jiawula deposit. (a) Fluid inclusion petrography shows that quartz intergrown with sphalerite in Sample 2-25. (b) Quartz veins cut the brecciated sphalerite in Sample 7-7. (c) Type 1 primary liquid-rich fluid inclusions. (d) Type 2 vapour-rich fluid inclusions appear only sporadically and might be the product of explosion [Colour figure can be viewed at wileyonlinelibrary.com]

TABLE 3 Fluid inclusion data in quartz from the Jiawula deposit

Host mineral	Sample no.	Measurements no.	Tm/°C	The average of Tm	Th/°C	The average of Th
Quartz	2-25	91	−1.4 to −0.2	−0.6	155.3–286.1	197.8
	7-7	44	−1.4 to −0.2	−0.5	169.4–285.6	205.6

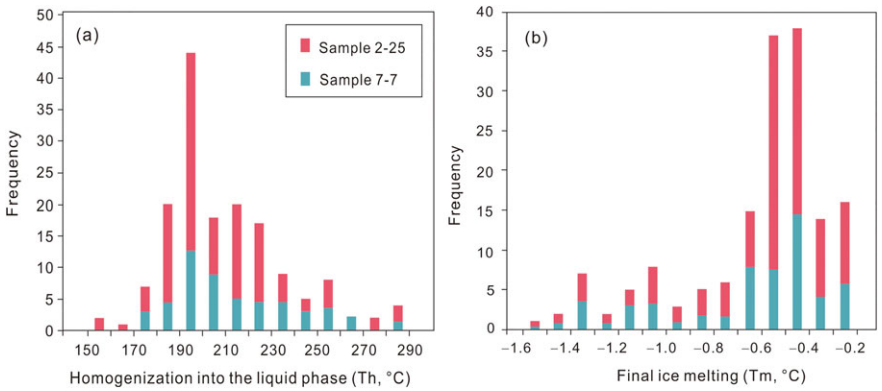

FIGURE 8 Histograms of (a) homogenization temperatures and (b) melting temperatures for primary aqueous fluid inclusions [Colour figure can be viewed at wileyonlinelibrary.com]

age of 131.88 ± 0.83 Ma of the muscovite in the Jiawula deposit indicate a later distinct hydrothermal event postdating the mineralization.

The Mongol–Okhotsk Ocean closure in the Middle Jurassic exerted some influence on the Great Xing'an Range area (Kravchinsky, Cogne, Harbert, & Kuzmin, 2002; Tomurtogoo, Windley, Kroner, Badarch, & Liu, 2005). The subduction direction of the Palaeo-Pacific Plate changed to the north or north-west at *ca.* 140 Ma (Mao et al., 2005; Maruyama, Isozaki, Kimura, & Terabayashi, 1997), causing large-scale delamination of the thickened continental crust and upwelling of the asthenosphere (Wang et al., 2006). The mineralization event occurred at *ca.* 143 Ma and might be attributed to the large-scale delamination and the Great Xing'an Range region was in an

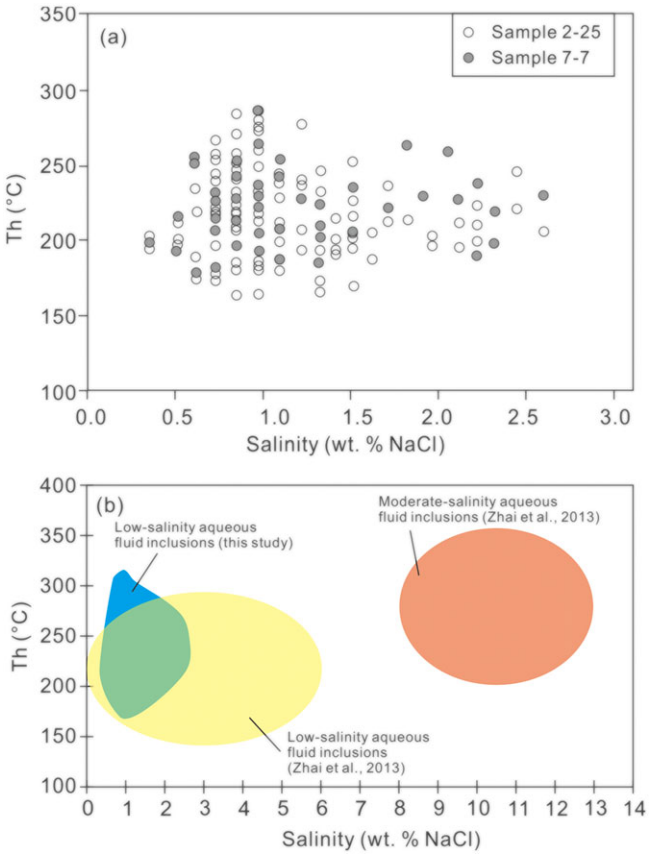

FIGURE 9 Plots of homogenization temperature and calculated salinity. (a) Data from this study. (b) A comparison of fluid inclusion data between this study and Zhai, Liu, Wang, Yao, Wu, et al., (2013) [Colour figure can be viewed at wileyonlinelibrary.com]

extensional environment during the Early Cretaceous period (Li et al., 2014; Niu et al., 2017; Yang, Guo, Song, Li, & He, 2015). The muscovite ^{40}Ar-^{39}Ar date of 133–131 Ma might be related to the response of the post-collisional extension.

8.2 | Fluid characteristics and evolution

Fluid inclusions were studied in quartz intergrown with ore minerals such as pyrite and sphalerite (Figure 7a), and in quartz veins that cut the brecciated sphalerite (Figure 7b). Although the occurrence of quartz in the two samples is obviously different, there is no marked difference in the distribution of the homogenization temperature and melting temperature of the fluid inclusions (Figures 8 and 9a). The final ice melting temperature and homogenization temperature data from both samples show relative concentration, with low temperature and low salinity, and there is no direct evidence of fluid mixing (Figure 9a; Dubessy, Derome, & Sausse, 2003). The low salinity and relatively low temperature of these fluids suggest a meteoric water or groundwater origin (Etoh, 2002).

A previous fluid inclusion study of the Jiawula deposit (Zhai, Liu, Wang, Yao, Wu, et al., 2013) demonstrates that the key factors allowing for metal transport and precipitation include the sourcing of magmatic fluids with high contents of metallogenic elements and the mixing of these hydrothermal fluids with meteoric waters resulting in the formation of a large Ag–Pb–Zn deposit (Figure 9b). Li et al. (2015) hold the view that fluid boiling is the dominant mechanism for the deposition of ore-forming materials.

Since the final ice melting temperatures show limited range, the boundaries of the distribution of the fluid evolution in the P–T phase diagram are constrained based on the fluid inclusions with the highest and lowest homogenization temperature (Figure 10). Different temperatures are used to be calculated for pressure correction (Table 4; Steele-Macinnis et al., 2012), which form the corresponding points along the isochores in Figure 10. Thus, the distribution range of the P–T conditions and the evolution of the fluid can be estimated. Assuming that the fluid evolved under constant pressure conditions, the cold meteoric water may react with the hot rocks, leading to an increase in temperature of the fluid and the rock cools down (Figure 10a). Another possibility is that under conditions of fluctuating fluid pressure, with the explosion or implicit explosion, the pressure decreases sharply (Figure 10b). The above two scenarios occur under ideal situation. In fact, the cooling effect is very widespread. The brecciated structure of sphalerite reflects the occurrence of explosive effect (Figure 3c,d), and the lattice texture of calcite also supports rapid cooling and crystallization under decompression condition (Figure 3e). Therefore, the fluid evolution of the Jiawula deposit is likely to be associated with both scenarios above.

Low-salinity fluids are often thought to be related with epithermal deposits, and groundwater or meteoric water plays an important role during mineralization process (Hedenquist, 1987; White & Hedenquist, 1995; Einaudi, Hedenquist, & Inan, 2003; Pirajno, 2009; Zhai, Liu,

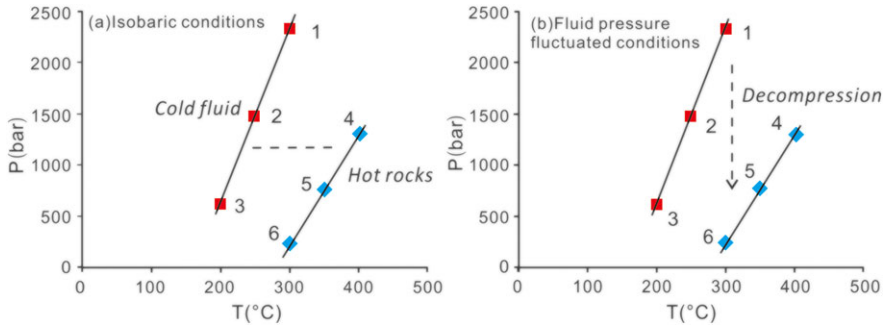

FIGURE 10 Isochores and possible models for fluid evolution in the Jiawula deposit under (a) isobaric conditions and (b) fluid pressure fluctuated conditions (values of the plots are corresponding to those in Table 4) [Colour figure can be viewed at wileyonlinelibrary.com]

TABLE 4 Isochore calculation of the fluid inclusions from the Jiawula deposit

No.	Tm	Phase	Th_{L-V}	Salinity wt% NaCl	Th (°C)	P homog. (bar)	$Density_{bulk}$ (g/cm_3)	dP/dT (bar/°C)	P correction based on:	T (°C)	Trapping conditions	
											T (°C)	P (bar)
1	−0.5	Ice	164	0.88	164.0	7	0.914	17.1	Temperature estimate	200	200	621
2	−0.5	Ice	164	0.88	164.0	7	0.914	17.1	Temperature estimate	250	250	1,475
3	−0.5	Ice	164	0.88	164.0	7	0.914	17.1	Temperature estimate	300	300	2,329
4	−0.5	Ice	286	0.88	286.0	70	0.739	10.7	Temperature estimate	300	300	220
5	−0.5	Ice	286	0.88	286.0	70	0.739	10.7	Temperature estimate	350	350	757
6	−0.5	Ice	286	0.88	286.0	70	0.739	10.7	Temperature estimate	400	400	1,293

Wang, Yao, Wu, et al., 2013). The fluid evolution in the Jiawula deposit characterized by low-salinity fluid, as well as cooling and decompression of groundwater or meteoric water appear to have been of significance for the mineralization.

8.3 | Spatial distribution of the metallogenic elements and exploration

A vertical projection of distribution of the metallogenic elements along the cross-section A-A′ is presented in Figure 4 (location of cross-section A-A′ is shown in Figure 2). Lead is concentrated in the northern part of the No. 2 ore body whereas it rarely occurs in the south (Figure 4b). Zn concentration is revealed in the north and central domains, and it is larger than that of Pb (Figure 4c), which may indicate that zinc is more active than lead during the transport and precipitation of metallogenic components. Besides, the range of sphalerite in the paragenesis of the Jiawula deposit is wider than that of galena (Niu et al., 2016), indicating the consistency of spatial and temporal distribution. The high value area of silver also occurs in the north and central parts, within the high anomaly domains of zinc and lead (Figure 4d). This also supports the notion that sphalerite and galena are the main carriers of silver in the Jiawula deposit.

In contrast to Pb, Zn, and Ag, the Cu grade contour map shows relative concentration of Cu in the southern part of the No. 2 ore body, showing increasing trend from the north to the south (Figure 4e). In the southern part of the Cu grade contour map, the unsealed contour suggests that copper may extend further southward. Chalcopyrite normally appears in the earlier stage of mineralization, and its formation temperature is relatively higher than sphalerite and galena (Niu et al., 2016). Copper is richer in the southern part of the No. 2 ore body, whereas lead, zinc, and silver are more concentrated in the middle and north, indicating that the temperature decreases from the south to the north. This reflects the spatial trend of the ore-forming elements, which also suggests the migration path of the ore-forming fluids from the south to the north.

The intrusion related to mineralization is located at the southern end of the No. 2 ore body, which can be regarded as the source of the heat and metallogenic components (Niu et al., 2017, 2016; Zhai, Liu, Wang, Yao, Wu, et al., 2013). The precipitation of ore-forming metals was initiated from high temperature such as copper in the south and then continued with the lower temperature elements such as lead, zinc, and silver in the north. This process is related with the cooling and decompression of the ore-forming fluids and the precipitation of the metallogenic elements.

9 | CONCLUSIONS

The $^{40}Ar/^{39}Ar$ plateau age of 133.27 ± 0.66 Ma and the $^{40}Ar/^{39}Ar$ isochron age of 131.88 ± 0.83 Ma of the muscovite in the Jiawula deposit indicate a discrete second hydrothermal event after mineralization, which can be correlated to post-collisional extension after the subduction direction of the Palaeo-Pacific Plate changed.

Fluid inclusions study shows characteristics of single components with relatively low temperature and low salinity, with no direct evidence of fluid mixing. Cooling and decompression might have played an important role on the mineralization of the Jiawula deposit with the dominant role of groundwater or meteoric water.

In the vertical projection map of the No. 2 ore body, lead, zinc, and silver are more concentrated in the northern and central domains, whereas the southern domain shows higher concentration of copper, reflecting the spatial trend of the ore-forming elements. Based on the precipitation temperature of the elements, we identify a decrease in temperature from the south to the north. The intrusion related to mineralization is located on the southern part of the No. 2 ore body, which might be the source of the heat and metallogenic components.

ACKNOWLEDGEMENTS

We thank the staff in Xin Barag Right Banner Rongda Mining Limited Liability Company for their valuable field support. This study is funded by National Key Research and Development Program of China (2016YFC0600210) and the China Geological Survey (12120114051101).

ORCID

M. Santosh https://orcid.org/0000-0002-1073-8477

REFERENCES

Bai, L. A., Sun, J. G., Gu, A. L., Zhao, K. Q., & Sun, Q. L. (2014). A review of the genesis, geochronology, and geological significance of hydrothermal copper and associated metals deposits in the Great Xing'an Range, NE China. *Ore Geology Reviews*, *61*, 192–203. https://doi.org/10.1016/j.oregeorev.2014.01.010

Cathles, L. M., Erendi, A. H. J., & Barrie, T. (1997). How long can a hydrothermal system be sustained by a single intrusive event? *Economic Geology*, *92*, 766–771. https://doi.org/10.2113/gsecongeo.92.7-8.766

Chen, Y. J., Zhang, C., Li, N., Yang, Y. F., & Deng, K. (2012). Geology of the Mo deposits in Northeast China. *Journal of Jilin University (Earth Science Edition)*, *42*, 1223–1268. (in Chinese with English abstract)

Ding, Q. (2004). Rapid complexometric titration of lead and zinc in ore. *Analytical Laboratory*, *23*(7), 63–65. (in Chinese with English abstract)

Dubessy, J., Derome, D., & Sausse, J. (2003). Numerical modelling of fluid mixings in the H_2O–NaCl system application to the North Caramal U prospect (Australia). *Chemical Geology*, *194*, 25–39. https://doi.org/10.1016/S0009-2541(02)00269-3

Einaudi, M. T., Hedenquist, J. W., & Inan, E. E. (2003). Sulfidation state of fluids in active and extinct hydrothermal systems: Transitions from porphyry to epithermal environments. *Special Publication-Society of Economic Geologists*, *10*, 285–314.

Etoh, J. (2002). Bladed quartz and its relationship to gold mineralization in the Hishikari low-sulfidation epithermal gold deposit, Japan. *Economic Geology*, *97*, 1841–1851. https://doi.org/10.2113/gsecongeo.97.8.1841

Foster, M. D. (1960). Interpretation of composition of trioctahedral micas. *U. S. Geological Survey Profesional Paper*, *354-B*, 11–49.

Ge, W. C., Wu, F. Y., Zhou, C. Y., & Abdel Rahman, A. A. (2005). Emplacement age of the Tahe granite and its constraints on the tectonic nature of the Ergun block in the northern part of the Da Hinggan Range. *Chinese Science Bulletin English Edition*, *50*, 2097–2105. https://doi.org/10.1360/982005-207

Hedenquist, J. W. (1987). Volcanic-related hydrothermal systems in the Circum-Pacific Basin and their potential for mineralisation. *Mining Geology*, *37*(205), 347–364.

Hu, S. K., Yan, H. Q., Ye, M., & Xiang, W. D. (1998). Metallogenic focus-area and superlarge mineral deposits in the bordering zones between China, Russia and Mongolia. *Science in China (Series D)*, *41*, 28–41. https://doi.org/10.1007/BF02875635

Kravchinsky, V. A., Cogne, J. P., Harbert, W. P., & Kuzmin, M. I. (2002). Evolution of the Mongol-Okhotsk Ocean as constrained by new palaeomagnetic data from the Mongol-Okhotsk suture zone, Siberia. *Geophysical Journal International*, *148*, 34–57. https://doi.org/10.1046/j.1365-246x.2002.01557.x

Kröner, A., Kovach, V., Belousova, E., Hegner, E., Armstrong, R., Dolgopolova, A., … Rytsk, E. (2014). Reassessment of continental growth during the accretionary history of the Central Asian Orogenic Belt. *Gondwana Research*, *25*(1), 103–125. https://doi.org/10.1016/j.gr.2012.12.023

Li, T., Wu, G., Liu, J., Hu, Y., Zhang, Y., Luo, D., & Mao, Z. (2015). Fluid inclusions and isotopic characteristics of the jiawula Pb–Zn–Ag deposit, Inner Mongolia, China. *Journal of Asian Earth Sciences*, *103*, 305–320. https://doi.org/10.1016/j.jseaes.2014.10.003

Li, T. G., Wu, G., Liu, J., Hu, Y. Q., Zhang, Y. F., & Luo, D. F. (2014). Rb-Sr isochron age of the Jiawula Ag-Pb-Zn deposit in the Manzhouli area and its geological significance. *Acta Petrologica Sinica*, *30*, 257–270. (in Chinese with English abstract)

Liu, J., Mao, J. W., Wu, G., Wang, F., Luo, D. F., & Hu, Y. Q. (2014). Zircon U–Pb and molybdenite Re–Os dating of the Chalukou porphyry Mo deposit in the northern Great Xing'an Range, China and its geological significance. *Journal of Asian Earth Sciences*, *79*, 696–709. https://doi.org/10.1016/j.jseaes.2013.06.020

Liu, J. M., Zhang, R., & Zhang, Q. Z. (2004). The regional metallogeny of Da Hinggan Ling, China. *Earth Science Frontiers*, *11*, 269–277. (in Chinese with English abstract)

Ludwig, K. R. (2004). *Isoplot/Ex, version 3.0: A geochronological tool kit for Microsoft Excel*. Berkeley, CA: Berkeley Geochronology Center.

Mao, J. W., Wang, Y. T., Zhang, Z. H., Yu, J. J., & Niu, B. G. (2003). Geodynamic settings of Mesozoic large-scale mineralization in North China adjacent areas. *Science in China (Series D)*, *46*, 838–851.

Mao, J. W., Xie, G. Q., Zhang, Z. H., Li, X. F., Wang, Y. T., Zhang, C. Q., & Li, Y. F. (2005). Mesozoic large-scale metallogenic pulses in North China and corresponding geodynamic settings. *Acta Petrologica Sinica*, *21*, 169–188. (in Chinese with English abstract)

Mao, J. W., Zhou, Z. H., Wu, G., Jiang, S. H., Liu, C. L., Li, H. M., … Liu, J. (2013). Metallogenic regularity and minerogenetic series of ore deposits in Inner Mongolia and adjacent areas. *Mineral Deposits*, *32*, 715–729. (in Chinese with English abstract)

Marsh, T. M., Einaudi, M. T., & McWilliams, M. (1997). $^{40}Ar/^{39}Ar$ geochronology of Cu-Au and Au-Ag mineralization in the Potrerillos district, Chile. *Economic Geology*, *92*, 784–806. https://doi.org/10.2113/gsecongeo.92.7-8.784

Maruyama, S., Isozaki, Y., Kimura, G., & Terabayashi, M. (1997). Paleogeographic maps of the Japanese Islands: Plate tectonic synthesis from 750 Ma to the present. *Island Arc*, *6*, 121–142. https://doi.org/10.1111/j.1440-1738.1997.tb00043.x

McDougall, I., & Harrison, T. M. (1999). *Geochronology and thermochronology by $^{40}Ar/^{39}Ar$ method* (p. 269). New York Oxford: Oxford University Press.

Nie, F. J., Li, Q. F., Liu, C. H., & Ding, C. W. (2015). Geology and origin of Ag-Pb-Zn deposits occurring in the Ulaan-Jiawula metallogenic province, northeast Asia. *Journal of Asian Earth Sciences*, *97*, 424–441. https://doi.org/10.1016/j.jseaes.2014.07.029

Niu, S. D., Li, S. R., Huizenga, J. M., Santosh, M., Zhang, D. H., Zeng, Y. L., … Zhao, W. B. (2017). Zircon U-Pb geochronology and geochemistry of the intrusions associated with the Jiawula Ag-Pb-Zn deposit in the Great Xing'an Range, NE China and their implications on mineralization. *Ore Geology Reviews*, *86*, 35–54. https://doi.org/10.1016/j.oregeorev.2017.02.007

Niu, S. D., Li, S. R., Santosh, M., Zhang, D. H., Li, Z. D., Shan, M. J., … Zhao, W. B. (2016). Mineralogical and isotopic studies of base metal sulfides from the Jiawula Ag-Pb-Zn deposit, Inner Mongolia, NE China. *Journal of Asian Earth Sciences*, *115*, 480–491. https://doi.org/10.1016/j.jseaes.2015.10.020

Ouyang, H. G., Mao, J. W., Santosh, M., Zhou, J., Zhou, Z. H., Wu, Y., & Hou, L. (2013). Geodynamic setting of Mesozoic magmatism in NE China and surrounding regions: Perspectives from spatio-temporal distribution patterns of ore deposits. *Journal of Asian Earth Sciences*, *78*, 222–236. https://doi.org/10.1016/j.jseaes.2013.07.011

Pirajno, F. (2009). Porphyry systems: Fossil and active epithermal systems. *Hydrothermal Processes and Mineral Systems. Springer Netherlands*, 355–533. https://doi.org/10.1007/978-1-4020-8613-7_5

Ronacher, E., Richards, J. P., Villeneuve, M. E., & Johnston, M. D. (2002). Short life-span of the ore-forming system at the Porgera gold deposit, Papua New Guinea: Laser $^{40}Ar/^{39}Ar$ dates for roscoelite, biotite, and hornblende. *Mineralium Deposita*, *37*(1), 75–86. https://doi.org/10.1007/s00126-001-0231-x

Selby, D., Creaser, R. A., Hart, C. J. R., Rombach, C. S., Thompson, J. F. H., & Smith, M. T. (2002). Absolute timing of sulfide and gold mineralization: A comparison of Re-Os molybdenite and Ar-Ar mica methods from the Tintina Gold Belt, Alaska. *Geology*, *30*, 791. https://doi.org/10.1130/0091-7613(2002)030<0791:ATOSAG>2.0.CO;2

Steele-Macinnis, M., Lecumberri-Sanchez, P., & Bodnar, R. J. (2012). HokieFlincs_H2O-NaCl: A Microsoft Excel spreadsheet for interpreting microthermometric data from fluid inclusions based on the PVTX

properties of H_2O-NaCl. *Computers & Geosciences*, *49*, 334–337. https://doi.org/10.1016/j.cageo.2012.01.022

Tang, J., Xu, W. L., Wang, F., Wang, W., Xu, M. J., & Zhang, Y. H. (2014). Geochronology and geochemistry of Early–Middle Triassic magmatism in the Erguna Massif, NE China: Constraints on the tectonic evolution of the Mongol–Okhotsk Ocean. *Lithos*, *184*, 1–16.

Tang, J., Xu, W. L., Wang, F., Zhao, S., & Wang, W. (2016). Early Mesozoic southward subduction history of the Mongol-Okhotsk oceanic plate: Evidence from geochronology and geochemistry of Early Mesozoic intrusive rocks in the Erguna Massif, NE China. *Gondwana Research*, *31*, 218–240. https://doi.org/10.1016/j.gr.2014.12.010

Tomurtogoo, O., Windley, B. F., Kroner, A., Badarch, G., & Liu, D. Y. (2005). Zircon age and occurrence of the Adaatsag ophiolite and Muron shear zone, central Mongolia: Constraints on the evolution of the Mongol-Okhotsk ocean, suture and orogen. *Journal of the Geological Society of London*, *162*, 125–134. https://doi.org/10.1144/0016-764903-146

Wang, D. H., Zheng, Z. H., Chen, Y. C., Tang, J. X., Li, J. K., & Ying, L. J. (2010). New data of the rock-forming and ore-forming chronology for China's important mineral resources areas. *Acta Geologica Sinica*, *84*, 1030–1040. (in Chinese with English abstract)

Wang, F., Zhou, X. H., Zhang, L. C., Ying, J. F., Zhang, Y. T., Wu, F. Y., & Zhu, R. X. (2006). Late Mesozoic volcanism in the Great Xing'an Range (NE China): Timing and implications for the dynamic setting of NE Asia. *Earth and Planetary Science Letters*, *251*, 179–198. https://doi.org/10.1016/j.epsl.2006.09.007

White, N. C., & Hedenquist, J. W. (1995). Epithermal gold deposits. Styles, characteristics and exploration. *SEG Newsletter*, *23*(1): 9–13.

Wilde, S. A., & Zhou, J. B. (2015). The late Paleozoic to Mesozoic evolution of the eastern margin of the Central Asian Orogenic Belt in China. *Journal of Asian Earth Sciences*, *113*, 909–921. https://doi.org/10.1016/j.jseaes.2015.05.005

Wu, F. Y., Sun, D. Y., Ge, W. C., Zhang, Y. B., Grant, M. L., Wilde, S. A., & Jahn, B. M. (2011). Geochronology of the Phanerozoic granitoids in northeastern China. *Journal of Asian Earth Sciences*, *41*, 1–30. https://doi.org/10.1016/j.jseaes.2010.11.014

Wu, G., Mi, M., Gao, F. J., Li, Z. Y., & Qiao, C. J. (2010). Ore-forming fluid characteristics and genesis of silver-lead-zinc deposits in the Manzhouli area, Inner Mongolia, China. *Earth Science Frontiers*, *17*, 239–255. (in Chinese with English abstract)

Wu, G., Sun, F. Y., Zhu, Q., Li, Z. T., Ding, Q. F., Li, G. Y., … Wang, H. B. (2006). Geological characteristics and genesis of gold deposits in Upper Heilongjiang Basin. *Mineral Deposits*, *25*, 215–230. (in Chinese with English abstract)

Yang, Y. T., Guo, Z. X., Song, C. C., Li, X. B., & He, S. (2015). A short-lived but significant Mongol–Okhotsk collisional orogeny in latest Jurassic–earliest Cretaceous. *Gondwana Research*, *28*, 1096–1116. https://doi.org/10.1016/j.gr.2014.09.010

Zeng, L. P. (2010). Geological features of Jiawula Ag-Pb-Zn deposit and its metallogenic control discussion. *Nonferrous Metals (Mining Section)*, *62*, 34–39. (in Chinese with English abstract)

Zhai, D. G., Liu, J. J., Wang, J. P., Yao, M. J., Liu, X. W., Liu, Z. J., … Li, Y. X. (2013). A study of stable isotope geochemistry of the Jiawula large Pb-Zn-Ag ore deposit, Inner Mongolia. *Earth Science Frontiers*, *20*, 213–225. (in Chinese with English abstract)

Zhai, D. G., Liu, J. J., Wang, J. P., Yao, M. J., Wu, S. H., Fu, C., … Li, Y. X. (2013). Fluid evolution of the Jiawula Ag–Pb–Zn deposit, Inner Mongolia: Mineralogical, fluid inclusion, and stable isotopic evidence. *International Geology Review*, *55*, 204–224. https://doi.org/10.1080/00206814.2012.692905

Zhai, D. G., Liu, J. J., Yang, Y. Q., Wang, J. P., Ding, L., Liu, X. W., & Zhang, H. Y. (2012). Petrogenetic and metallogentic ages and tectonic setting of the Huangganglang Fe-Sn deposit, Inner Mongolia. *Acta Petrologica et Mineralogica*, *31*, 513–523. (in Chinese with English abstract)

Zhao, P., Xu, B., & Zhang, C. (2017). A rift system in southeastern Central Asian Orogenic Belt: Constraint from sedimentological, geochronological and geochemical investigations of the Late Carboniferous-Early Permian strata in northern Inner Mongolia (China). *Gondwana Research*, *47*, 342–357. https://doi.org/10.1016/j.gr.2016.06.013

Zhao, Q. Q., Sun, C. B., Jing, L. H., & Wang, D. P. (2005). Application of structure geochemistry discrimination analysis for prospecting: Taking the Jiawula silver polymetallic deposit in Hulunbeier league as an example. *Mineral Resources and Geology*, *19*, 414–417. (in Chinese with English abstract)

Zheng, D. Q. (1991). Discussion on the vertical projection of the ore body when the orientation of the exploration line changes greatly. *Henan Geology*, *1991*(1), 55–59. (In Chinese with English abstract)

Zheng, Y., Zhang, L., Chen, Y. J., Hollings, P., & Chen, H. Y. (2013). Metamorphosed Pb–Zn–(Ag) ores of the Keketale VMS deposit, NW China: Evidence from ore textures, fluid inclusions, geochronology and pyrite compositions. *Ore Geology Reviews*, *54*, 167–180. https://doi.org/10.1016/j.oregeorev.2013.03.009

Zhou, J. B., & Wilde, S. A. (2013). The crustal accretion history and tectonic evolution of the NE China segment of the Central Asian Orogenic Belt. *Gondwana Research*, *23*(4), 1365–1377. https://doi.org/10.1016/j.gr.2012.05.012

Zhou, J. B., Wilde, S. A., Zhang, X. Z., Zhao, G. C., Zheng, C. Q., Wang, Y. J., & Zhang, X. H. (2009). The onset of Pacific margin accretion in NE China: Evidence from the Heilongjiang high-pressure metamorphic belt. *Tectonophysics*, *478*, 230–246. https://doi.org/10.1016/j.tecto.2009.08.009

Zhou, Z., Mao, J., Liu, J., Ouyang, H., Che, H., & Ma, X. (2015). Early Cretaceous magmatism and ore mineralization in Northeast China: Examples from Taolaituo Mo and Aobaotu Pb-Zn deposits. *International Geology Review*, *57*, 229–256. https://doi.org/10.1080/00206814.2014.1002117

Zhou, Z. H., Mao, J. W., & Lyckberg, P. (2012). Geochronology and isotopic geochemistry of the A-type granites from the Huanggang Sn-Fe deposit, southern Great Hinggan Range, NE China: Implication for their origin and tectonic setting. *Journal of Asian Earth Sciences*, *49*, 272–286. https://doi.org/10.1016/j.jseaes.2012.01.015

SUPPORTING INFORMATION

Additional supporting information may be found online in the Supporting Information section at the end of the article.

How to cite this article: Niu S-D, Li S-R, Huizenga JM, Santosh M, Zhang D-H, Li Z-D. $^{40}Ar/^{39}Ar$ geochronology, fluid inclusions, and ore-grade distribution of the Jiawula Ag–Pb–Zn deposit, NE China: Implications for deposit genesis and exploration. *Geological Journal*. 2020;55:1115–1127. https://doi.org/10.1002/gj.3473